Cubic Cu2O nanoparticles decorated on TiO2 nanofiber heterostructure as an excellent synergistic photocatalyst for H2 production and sulfamethoxazole degradation

Cubic Cu_2O nanoparticles decorated on TiO_2 nanofiber heterostructure as an excellent synergistic photocatalyst for H_2 production and sulfamethoxazole degradation

Karthikeyan Sekar, [a,b*] Chitiphon Chuaicham, [a†] Balakumar Vellaisamy, [a†] Wei Li,[c] Wei Zhuang,[d] Xiaohua Lu,[e] Bunsho Ohtani,[f] Keiko Sasaki, [a,f*]

[a]*Department of Earth Resources Engineering, Faculty of Engineering, Kyushu University, 744 Motooka, Nishiku, Fukuoka 819-0395, Japan*

[b] *Department of Chemistry and Biotechnology, School of Engineering, The University of Tokyo, 7-3-1 Hongo, Bunkyo-ku, Tokyo 113-8656, Japan*

[c]*School of Engineering, Institute for Materials & Processes, The University of Edinburgh, Robert Stevenson Road, Edinburgh EH9 3FB, United Kingdom.*

[d]*State Key Laboratory of Materials-Oriented Chemical Engineering, Nanjing Tech University, Nanjing 211816, China.*

[e]*College of Chemical Engineering, State Key Laboratory of Materials-oriented Chemical Engineering, Nanjing Tech University, Nanjing, 211816, PR China.*

[f]*Institute for Catalysis, Hokkaido University, Sapporo 001-0021, Japan*

*Corresponding Author: E-mail: k-sekar@chembio.t.u-tokyo.ac.jp; keikos@mine.kyushu-u.ac.jp; Tel: +81-92-802-3338. *† C.C. and B.V. contributed equally to this work.*

Abstract

We report a simple strategy for providing a homogenous TiO_2 nanofibre host environment to stabilize Cu_2O nanoparticles with an average size of ~60 nm and high dispersibility. We found that the small fraction of Cu_2O nanoparticles in direct contact/partially submerged with TiO_2 nanofibre arrays (diameter ~300 nm and length ~650 nm) showed excellent synergistic photocatalytic performance for an H_2 production rate of 48 μmol g^{-1} h^{-1} with an apparent quantum efficiency of 3.6 %. The H_2 production rate was much higher (factor of ~6.5 times) compared with unmodified TiO_2-NF. In addition, the synergistic Cu_2O/TiO_2-NF photocatalyst showed significant oxidative-degradation of sulfamethoxazole (7×10^{-2} mmol g^{-1} min^{-1}) and was highly stable during five cycles. The small fraction of Cu_2O nanoparticles are well dispersed and form heterojunction interfaces to promote charge transfer and provide active sites. This argument is verified by morphology characterisation, band alignment, energy-resolved distribution of electron traps, electrochemical transient photocurrent, and electrochemical impedance (EIS). In addition, a detailed discussion is provided regarding the surface and bulk elemental composition determined by X-ray photoelectron spectroscopy (XPS), X-ray fluorescence (XRF), and X-ray absorption near edge structure (XANES).

Keywords: *Cu_2O/TiO_2-nanofibre, photocatalysts, hydrogen production, sulfamethoxazole visible light.*

1. Introduction

For efficient solar energy usage, there has been interest in heterogeneous catalysts for various photocatalytic applications, such as water splitting to produce H_2, CO_2 reduction into solar fuels, fine chemical production and organics decomposition reactions [1]. In the last few decades, TiO_2 has been considered the most promising benchmark photocatalyst in various applications [2]. However, titanium dioxide activates only 5 % of the UV light region because of the wide bandgap (Eg 3.2 eV) and also easily recombines the photoinduced charge carrier, which limits the successful utilization of solar light in practical applications [3].

To achieve high-efficiency photocatalytic activity and charge separation of TiO_2, methods in the literature including integrating co-catalysts or modification with narrow band gap semiconductors [4, 5]. Among the semiconducting co-catalysts, copper oxide (Cu_2O) is an economical and earth rich p-type semiconductor (band gap of 2.0 to 2.4 eV) with favourable valence and conduction band positions for effective photocatalytic activity in numerous research areas, such as water splitting and organics decomposition [6, 7], CO_2 reduction, etc., towards the visible region [8, 9]. However, stability of Cu_2O is a major limitation under light illumination due to photocorrosion.

The combination of these two materials (p-Cu_2O and n-TiO_2) has great advantage and overcomes the Cu_2O photocorrosion for efficient photocatalytic performance [10, 11]. Additionally, the band energy gap of Cu_2O is lower than that of TiO_2, and both the valence band and conduction band positions are above those of TiO_2, which enables excellent charge transfer and separation processes in the photogenerated carriers to improve the photo response and lifetime of the charge carrier [12]. In addition, the heterojunction formation at the interface of p-Cu_2O/n-TiO_2 creates a build-in-inner electrostatic field and might improve the electron-hole pair separation. There are many reports on the Cu_2O/TiO_2 heterojunction, such as defect modulation [13], Quantum dot TiO_2 [14], controlled facets [15], and TiO_2 nanotube arrays [12] for various photocatalytic applications. Interfacial interaction of the co-catalyst, electronic band structures and the intrinsic light-absorption of the catalyst are important parameters for efficient and stable photocatalytic applications.

It is still a challenge to understand the interface formation and interfacial interaction when p-Cu_2O and n-TiO_2 combine. A particular mesoporous nanofibre TiO_2 we had developed previously can be an excellent host for incorporation of metal nanoparticles due to its pore arrangement, providing a homogenous surface for stabilizing nanoparticles with high dispersibility [16]. Meanwhile, our other recent work [17-19] reported that size and morphology controlled Cu_2O nanostructures can be design and synthesised without the needs of surfactants which commonly lead to severe hindrance of active sites and thus photocatalytic performance [20-23].

The combination of these two materials will provide a synergistic photocatalyst for enhanced performance and a perfect platform to reveal their interface formation and interfacial interaction. Here, we report a simple strategy for the partially submerged ultrafine Cu_2O (20-100 nm) nanoparticles decorated/modified on the TiO_2 nanofibre (diameter ~300 nm and length

~650 nm) architecture, which significantly improved the surface electronic and optical properties, yielding an excellent synergistic visible-light photocatalyst.

We have found that the small fraction of Cu_2O nanoparticle surface in direct contact with the TiO_2 nanofibre arrays showed excellent photocatalytic H_2 production and sulfamethoxazole (as a model antibiotic organic molecule) oxidative-degradation applications. Detailed discussion is provided regarding the Cu_2O nanoparticle growth on TiO_2 nanofibre structure, Cu_2O/TiO_2-NF interfacial interaction, and surface and bulk elemental composition determined by XPS, XRD, XRF, and XANES. Energy-resolved Distribution of Electron Traps (ERDT) near the conduction band bottom position (CBB) of TiO_2, TiO_2-NF and Cu_2O/TiO_2-NF composites using reversed double-beam photoacoustic spectroscopy (RDB-PAS) were investigated for the first time. The interfacial interaction was confirmed by band alignment, and the charge carrier mechanism was confirmed by electrochemical transient photocurrent and EIS. In addition, by-products of sulfamethoxazole decomposition were identified (LC/MS/MS) and, finally, stability of the catalysts are discussed in detail.

2. Experimental section

2.1. Anatase TiO_2 Nanofibre (TiO_2-NF) synthesis

$K_2Ti_2O_5$ powders with water were taken for a hydration reaction after that aqueous solution of HCl (0.5 mol/L) was added into the above reaction mixture for ion exchange for the formation of hydrated titanate ($H_2Ti_2O_5$). The solid-aqueous products were separated by filtration, washed several times with deionised water, and then dried at 60°C in an oven under vacuum. Inductively coupled plasma-mass spectrometry (ICP-MS) was used to measure the final residual K^+ ions, which were found to be less than 0.2 wt%. Finally, the hydrated $H_2Ti_2O_5$ was calcined at 500°C in a muffle oven for 2 h to attain anatase TiO_2-NF.

2.2. Cu_2O decoration on the TiO_2 Nanofibre structure

Well-defined size-controlled Cu_2O nanoparticles on TiO_2 nanofibre were synthesised at different temperatures (50 to 100°C). For example, Cu_2O synthesized by 0.1 M copper acetate monohydrate (2 mL) was mixed with 90 mg of TiO_2 nanostructure with 5 mL of distilled water, which was stirred at 50°C-100°C for 10 min. In a separate vessel, 1 M NaOH (0.8 mL) and 0.2 M ascorbic acid (0.8 mL) were taken to initiate the redox reaction. The mixture of NaOH/ascorbic acid was then quickly added to the above copper acetate/TiO_2 reaction mixtures under continued stirring for 5 min. The reactions of solid-liquid mixtures were shifted to a centrifuge tube and then separated into whitish-yellow Cu_2O/TiO_2-NF precipitate.

2.3. Reversed Double-Beam Photoacoustic Spectroscopy (RDB-PAS)

The synthesized photocatalysts of Cu_2O/TiO_2-NF products were taken, approximately 200 mg, and added into a PAS cell equipped with an electret condenser microphone and a quartz window on the upper side under N_2 flow saturated with methanol vapour for at least 30 min. A light beam from an Xe lamp with a grating monochromator modulated at 80 Hz by a light

chopper was irradiated from 650 nm to 350 nm through the cell window to detect the PAS signal using a digital lock-in amplifier. The energy-resolved distribution of electron traps (ERDT) was obtained by determining the amount of photoabsorption change for the accumulated electrons [24, 25].

2.4. Photoelectrochemical Characterization

Three electrode photoelectrochemical cells were used in this experiment, the counter electrode was a Pt wire, and Hg/Hg_2SO_4 was used for the reference electrode. The working electrode of glassy carbon electrode (GC) was constructed by dropcasting 5 µL of homogeneous colloid on a 3-mm dia in the GC electrode. The working electrode was prepared by synthesised catalysts made of colloid mixtures by 30-minute sonication of catalysts with Nafion dispersed in a water/ethanol mixture (0.5 mL, 1:1 v/v). A 200-W Hg-Xe arc lamp (plus a λ>420 nm cut-off filter) was used as the light source. Autolab potentiostat with Nova software was used for electrochemical measurements. Nyquist plots were recorded using a 10-mV AC signal between 100 kHz and 0.1 Hz in frequency. Mott Schottky plots of the synthesised products were measured at a frequency of 1000 Hz under a DC signal over a potential range of -1 to 0 V with a potential step of 10 mV.

2.5. Photocatalytic H_2 evolution

Photocatalytic H_2 production was carried out using synthesised Cu_2O, TiO_2-P25, TiO_2-NF and their composites in a sealed quartz photoreactor. Photocatalytic H_2 evolution experiments was carried out in 20 mg of catalysts dispersed into 50 mL of deionised water with 2 mL of methanol as a sacrificial electron donor under sonication for 5 min for uniform distribution. The gas was purged for 1 h prior to light irradiation to remove the excess oxygen in the reactor. Gas samples before and after the reaction mixtures were withdrawn periodically in a 1-mL airtight syringe to determine the H_2 production by gas chromatography.

2.6. Sulfamethoxazole (SMX) photodegradation experiment

Typically, 20 mg of Cu_2O and Cu_2O/TiO_2-NF products were dispersed in 50 mL of SMX (0.01184 mM) in a 250-mL quartz cell photoreactor and then sonicated for 10 min to complete dispersion. Before photoreaction, the above mixtures of the reaction were performed in a dark condition to ensure any adsorption and sample was collected for HPLC analysis. After 1 hr of adsorption, samples were periodically collected and filtered using a CPO20AN filter for HPLC analysis. The SMX removal efficiency was calculated according to **equation 1** as follows:

$$\text{SMX removal (\%)} = \frac{\text{SMX initial} - \text{SMX final}}{\text{SMX initial}} \times 100 \qquad \mathbf{1}$$

2.7. HPLC analysis of SMX

The SMX concentration was analysed using a high-performance liquid chromatography system (JASCO UV plus 2075 serious, Japan) coupled with an intelligent UV/Vis detector selected at λ=254 nm and a Shodex C18M 4E analytical column (4.6 I.D × 250 mm). Separation factor (α1=2.42 and α2=1.47) with a constant temperature of 25°C, pressure maximum of 20 MPa,

and pressure minimum of 0.2 MPa. The eluent consists of 60:10:30 (v/v) acetonitrile:water:formic acid (25 mM) (TCI, Japan) with a flow rate of 0.6 mL/min.

3. Results and discussion

3.1. Catalyst characterization

The formation of size-controlled cubic Cu_2O nanoparticles on TiO_2-NF is displayed in **Scheme 1**. As shown in the scheme, 0.1 M copper acetate monohydrate (2 mL) was mixed with 90 mg of TiO_2 nanofibre nanostructure with 5 mL of distilled water, and the mixtures were thoroughly mixed using ultrasonication to obtain the Cu(II)-TiO_2-NF complex; Cu^{2+} ions penetrated and diffused into the TiO_2 nanofibre structure under air atmosphere due to expulsion [10]. In the second step, the complexed/diffused Cu(II) ions were precipitated for copper hydroxide, followed by reduction to Cu(I) oxide by adding alkaline NaOH/ascorbic acid mixture at 60°C under stirring. The cubic Cu_2O nanoparticles are in a size range of 20-100 nm (more SEM and TEM images are shown later in **Fig. 2 and 3** and also in supporting materials **Fig. S1**). However, in contrast, when TiO_2-NF is absent, Cu_2O particles self-aggregated to form agglomerated Cu_2O nanoparticles (~400 nm), indicating that the Cu_2O size was better controlled using TiO_2 nanofibre. This is a great advantage comparing to the use of additional templates/surfactants, which will introduce impurities unavoidably block Cu_2O active surface sites and reduce the catalytic activity in the surface-related reactions [26, 27].

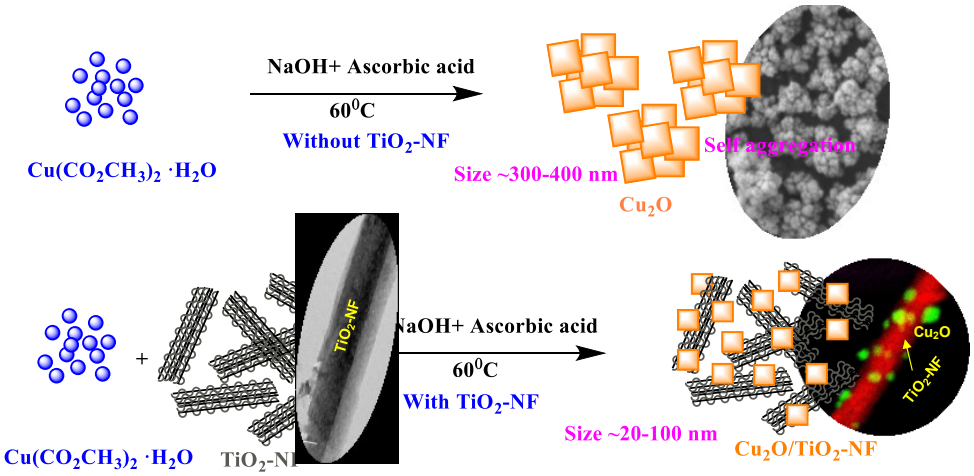

Scheme 1 Synthetic diagram for the construction of Cu_2O and Cu_2O/TiO_2-NF (60°C) nanocomposite.

Fig. 1 shows the PXRD patterns of Cu_2O/TiO_2-NF nanocomposites as well as Cu_2O and TiO_2-NF references. The XRD pattern of Cu_2O showed the reflection at 2θ = 29.58 (3.01 Å), 36.44(2.46 Å), 42.33(2.13 Å), 61.41 (1.50 Å), and 73.56 (1.28 Å) corresponding to the (1 1 0), (1 1 1), (2 0 0), (2 2 0), and (3 1 1) planes, which indicated the cubic cuprite (Cu_2O) phase (with space group *Pn-3m*, no. 224) and cell parameters of a = 4.27, b = 4.27, c = 4.27, and β = 90.38 (JCPDS number 01-071-3645). The XRD pattern of TiO_2-NF showed the diffraction at 2θ = 25.30 (3.52A), 38.50 (2.33A), 48.04 (1.89A), 53.88 (1.70A), 55.06 (1.66A), 62.75 (1.48A), and 75.04 (1.26A) corresponding to the (101), (112), (200), (105), (211), (204), and

(215) planes, which indicated a tetragonal crystal system of TiO_2-NF anatase with space group *I41/amd (141* and cell parameters of $a = 3.78$, $b = 3.78$, $c = 9.51$, and $\beta = 90.0$ (JCPDS number 03-065-5714).

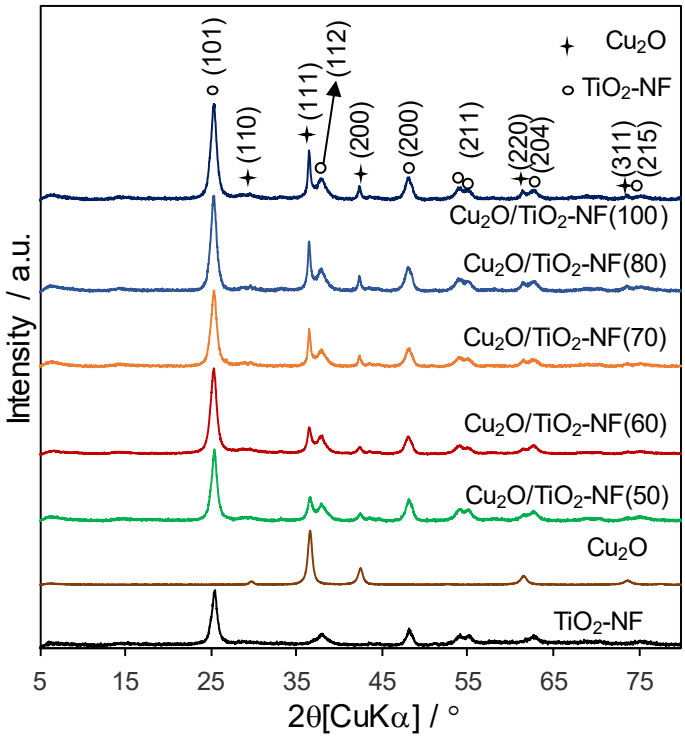

Fig. 1 Powder XRD patterns spectrum of Cu_2O, TiO_2-NF and their composites (50 to 100°C).

Patterns of Cu_2O/TiO_2-NF nanocomposites at diverse temperatures clearly demonstrate the characteristic planes of the TiO_2-NF anatase phase and low but observable Cu_2O peaks, indicating that the cuprite nanoparticles were evenly distributed on the TiO_2-NF structure [28]. From the XRD patterns, no other characteristic impurities such as $Cu(OH)_2$ and others were found, indicating that the composites contain only Cu_2O and TiO_2-NF. The crystalline sizes were calculated using the Scherrer equation, and the phase compositions of the Cu_2O/TiO_2-NF composites were analysed by the Rietveld method displayed in **Table 1**.

Fig. 2 displays high-resolution TEM images of well-dispersed/submerged Cu_2O nanoparticles (20-100 nm) on the TiO_2 nanofibre (diameter ~300 nm and length ~650 nm) structure in the Cu_2O/TiO_2-NF (60°C) sample. **Fig. 2a** clearly shows that the lattice d-spacing of 0.26 nm corresponds to the d_{111} planes of Cu_2O and, the d-space of 0.23 nm and 0.35 nm corresponds to the d_{112} and d_{101} anatase phase of TiO_2-NF, which is in good agreement with XRD patterns. In addition, images in **Fig. 2c-e** and **Fig. S3a-e** clearly indicate that the Cu_2O nanoparticles interpenetrated as well as partially submerged into the TiO_2 nanofibre surface.

On the Cu_2O/TiO_2-NF (60°C) sample, scanning transmission electron microscopy (STEM) combined with energy-dispersive X-ray spectroscopy (EDS) images clearly evidenced the even distribution of Cu_2O nanoparticles (20 to 100 nm) on the TiO_2 nanofibre surface (**Fig. 3a-g**). Elemental analysis shows ~10% Cu atom and ~53% Ti atom, as presented in **Fig. 3g and 3h**.

FE-SEM images of Cu_2O/TiO_2-NF prepared at different temperatures (50 to 100°C) are shown in **Fig. S2a-e**. It can be noted that, with the increase of temperature, the density of the Cu_2O nanoparticles increased, and they agglomerated on the TiO_2-NF surface. The increase in the amount of Cu_2O nanoparticles with increasing temperature is in good agreement with the XRF results (**Table 1**).

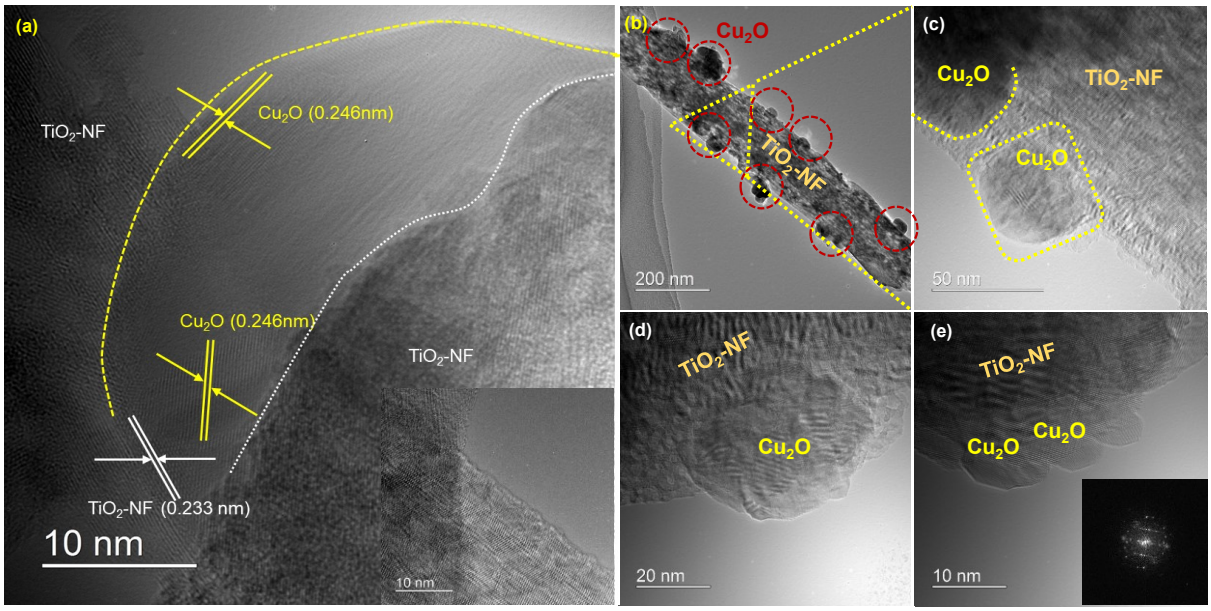

Fig. 2 a-e) HR-TEM images of Cu_2O/TiO_2-NF (60°C) captured an Ultra-scan camera.

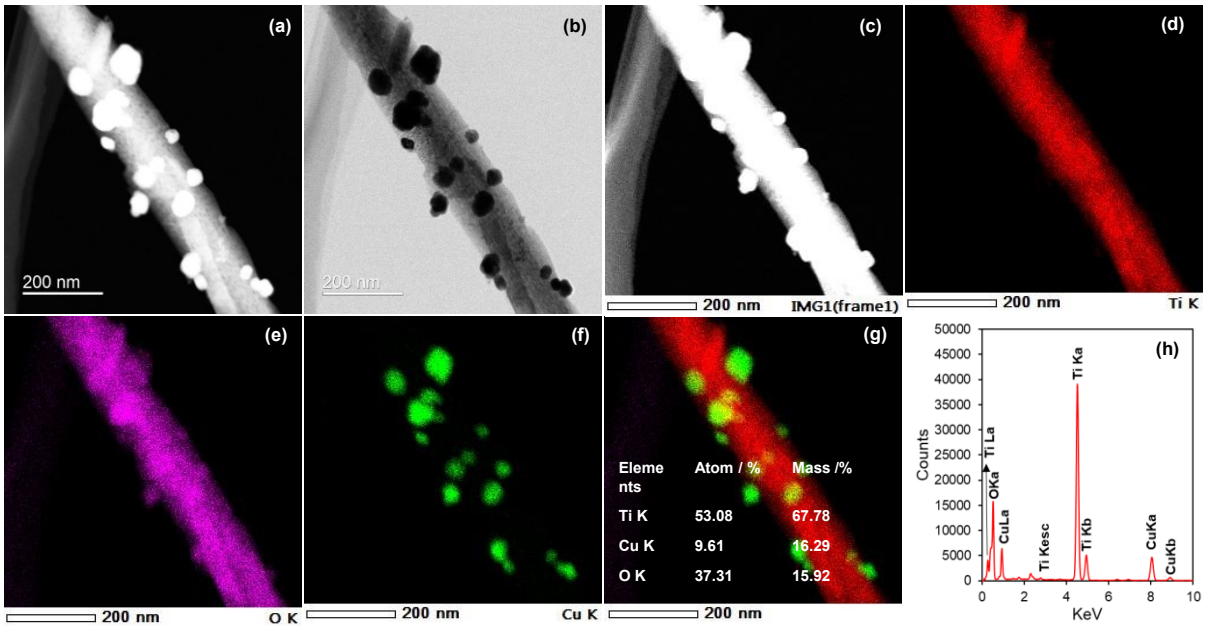

Fig. 3 a-g) STEM and elemental mapping of synthesised Cu_2O/TiO_2-NF (60°C).

The optical absorption and electronic characteristic of synthesised Cu_2O, TiO_2 and their composites were observed by DR UV-vis spectra, as shown in **Fig. 4**. The DR UV-vis spectra of Cu_2O showed a broad light absorbance due to interband absorption consistent with reports

[29, 30], while the TiO_2-NF showed only in the UV region ~380 nm. The composites show a combination of the two individuals. The corresponding band gap energies were calculated using Tauc plots, as shown in **Fig. S4** and the following **Eq. (2):**

$$\alpha hv = A(hv - E_g)^{\eta} \quad \textbf{2}$$

where α is the linear absorption coefficient, A is the absorption coefficient, h is Planck's constant, hν is the photon energy, and Eg is the band gap. The energy gap of synthesised Cu_2O, TiO_2-NF and their composites were also obtained from the Kubelka-Munk function presented as **Eq. (3):**

$$a = \frac{(1-R)^2}{2R} \quad \textbf{3}$$

From the KM function, the calculated direct band gap (Eg) values of 2.46 eV for Cu_2O, indirect band gap of 3.17 eV for TiO_2-NF, and their composites are presented **in Table 1**. Results from Tauc plots agreed very well with those from KM function.

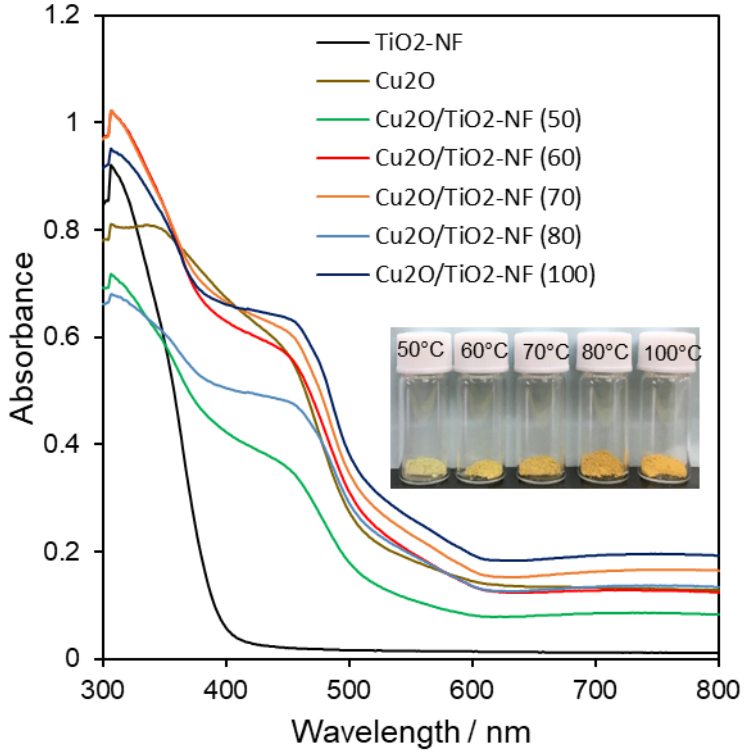

Fig. 4 DR UV-vis spectra of Cu_2O, TiO_2-NF and their composites (50 to 100°C).

It is clear that the combination of Cu_2O and TiO_2-NF has greatly influenced the band gap energies of the synthesised composites, which should be due to the interfacial interaction between Cu_2O and TiO_2-NF, as well as the intrinsic exciton band and d-d transition of Cu species. For example, the absorption range of 385 to 515 nm might due to the interfacial charge transfer (IFCT) of the TiO_2 valence band to Cu_xO- aggregates [28]. As a result, the Cu_2O/TiO_2-NF composites show strong visible light absorption properties to be ready to perform enhanced photocatalytic efficiency.

Table 1 Physicochemical properties of synthesised Cu_2O, TiO_2-NF and their composites

Catalyst	Cu_2O Crystalline size (nm)[a]	Composition of Cu_2O (%) [b]	Composition of Cu_2O at surface (%) [c]	Composition of Cu_2O in the bulk (%) [d]	Band gap (eV)[e]	BET surface area ($m^2 g^{-1}$) [f]	Total pore volume ($cm^3 g^{-1}$) [f]	VB edge potential (eV) [g]	CB edge potential (eV)[g]
TiO_2-NF	11.59	-		-	3.17	79.49	0.275	1.69	-1.48
Cu_2O	14.87	-		-	2.46	15.2	0.190	0.23	-2.23
Cu_2O /TiO_2-NF (50)	13.34	11.23	31.7	14.85	2.52	67.25	0.266	1.13	-1.39
Cu_2O /TiO_2-NF (60)	15.28	11.85	22.9	15.59	2.48	67.82	0.251	0.78	-1.70
Cu_2O /TiO_2-NF (70)	16.31	12.04	23.2	16.92	2.48	61.1	0.264	0.54	-1.94
Cu_2O /TiO_2-NF (80)	24.1	14.79	23.8	17.04	2.42	58.7	0.262	0.32	-2.10
Cu_2O /TiO_2-NF (100)	24.7	14.81	25.3	19.89	2.40	55.26	0.261	0.28	-2.12

[a]Scherrer equation, [b]Rietveld method, [c]XPS, [d]X-ray fluorescence, [e]Tauc plots, [f]N_2 porosimetry, [g]VB XPS and DR UV-vis.

To elucidate the surface structure properties of the Cu_2O/TiO_2-NF composites, all of the samples were characterized using RDB-PAS. **Fig. 5** shows the ERDT/CBB patterns from EDB-PAS of each sample plotted as a function of energy from the VBT vs. electron-trap density. The ERDT/CBB patterns of TiO_2-NF and TiO_2-P25 (anatase phase of TiO_2) show the high electron accumulation density approximately centred at 3.1 eV. Interestingly, the ERDT/CBB patterns of the composites all shifted to higher energy around 3.3 eV. The extent of shifting

increased when the synthetic temperature increased. The shifting of ERDT/CBB patterns indicates the distortion of the surface of TiO_2-NF by impanation of Cu_2O to form heterojunction with TiO_2-NF. The ERDT/CBB patterns of the composite are in good agreement with the TEM observation which shows that the surface of TiO_2 was modified by Cu_2O.

The surface oxidation states of synthesised Cu_2O and their Cu_2O/TiO_2-NF products were observed using core-level Cu 2p, Ti 2p X-ray photoelectron spectroscopy (XPS) shown in **Fig. S5**. The XPS binding energy peak of 458.5 eV and 464.1 eV, consisted with characteristic peak of Ti $2p_{3/2}$ and Ti $2p_{1/2}$ in TiO_2-nanofibre and binding energy peaks at 931.4 eV and 951.2 eV, consisted to Cu $2p_{3/2}$ and Cu $2p_{1/2}$ spin-orbit split of Cu/Cu_2O; the weak binding energy at 934.3eV and 954.1 eV with satellite shakeup at 941 eV, in all the synthesised products corresponds to CuO [31]. The characteristic of strong shakeup features was due to the unoccupied $3d^9$ shell arrangement of Cu^{2+} species, while the presence of CuO prevented the surface stability of Cu_2O to further oxidation [32]. The surface Cu(I): Cu(II) composition form XPS results also consistent with the XRD Rietveld method and XRF results.

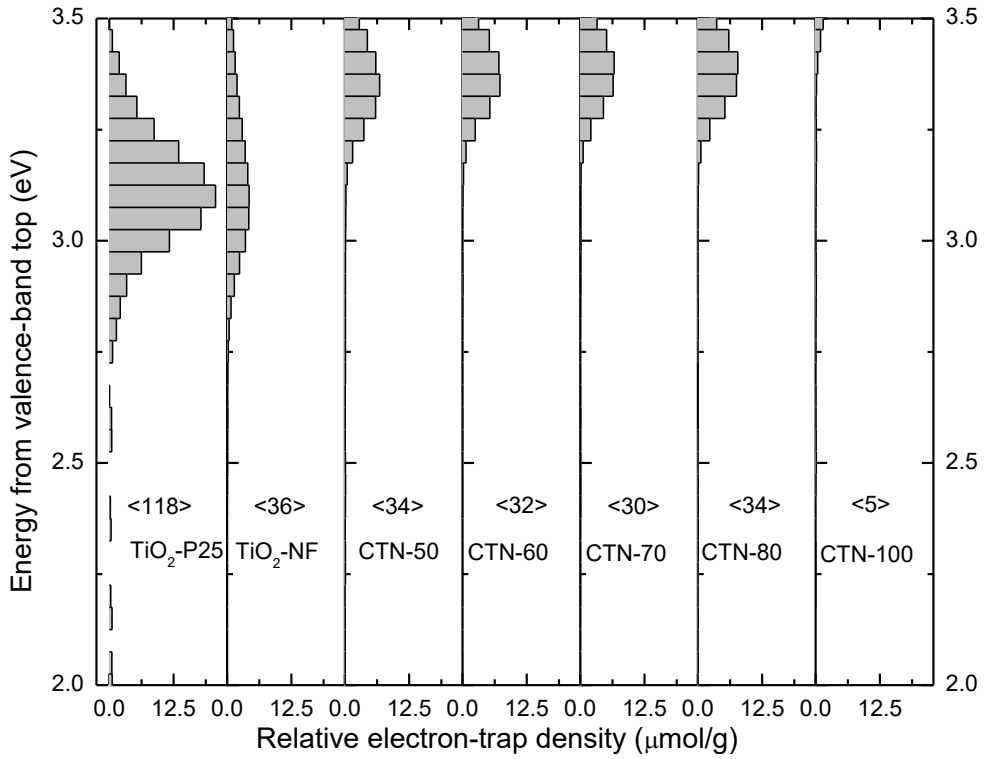

Fig. 5 ERDT pattern of TiO_2, TiO_2-NF and Cu_2O/TiO_2-NF products, named CTN, from 50 to 100°C.

The "fingerprint" of X-ray absorption near edge structure (XANES) spectroscopy was measured to further investigate the Cu_2O or CuO compositions in the synthesised products. The Cu K-edge XANES were analysed for Cu_2O samples, as well as synthesised Cu_2O/TiO_2-NF composites, which are compared with standards in **Fig. 6A** (Cu-metal, Cu_2O and CuO). Quantitative compositions obtained from linear combination fitting (LCF) are presented in **Table S1**. The formation of both Cu^+ (> 70%) and Cu^{2+} (< 30%) species on the TiO_2 surface was further consistent with reported literature [4].

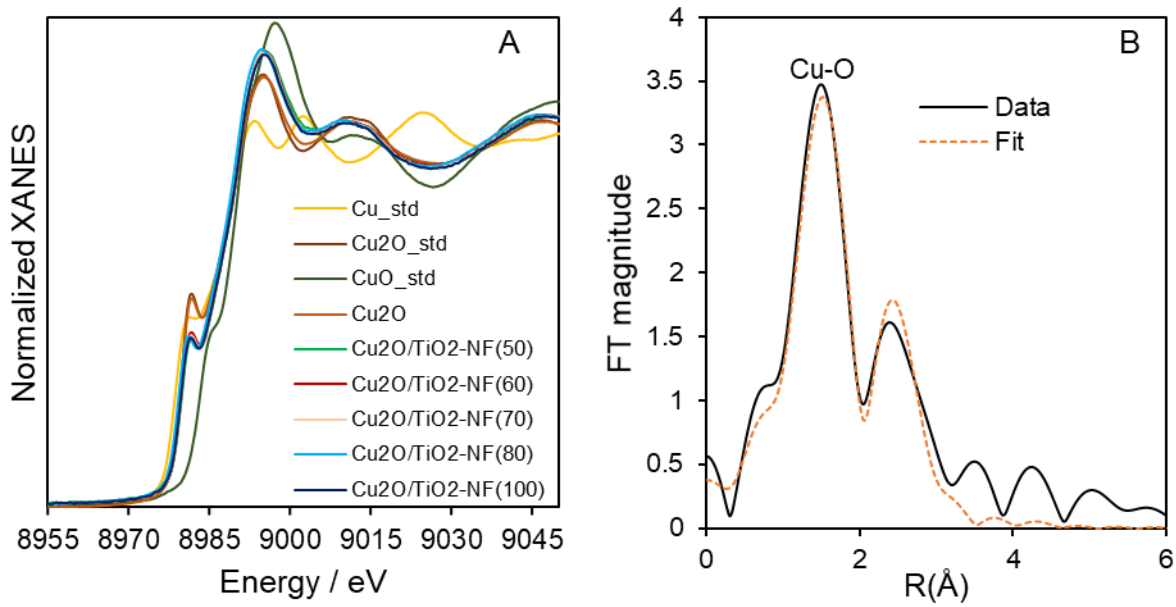

Fig. 6 A Cu K-edge XANES spectra of Cu_2O, Cu_2O/TiO_2-NF (50 to 100°C) and reference materials, B) Cu K-edge EXAFS spectra of Cu_2O/TiO_2-NF (60°C) in k space.

The presence and property of Cu_2O in the Cu_2O/TiO_2-NF (60°C) was further studied by extended X-ray-absorption fine-structure (EXAFS) analysis in Cu k-edge. The fitting is in good agreement with real parts of Fourier transform spectra, as shown in **Fig. 6B** and **Fig. S6**. The fitting clearly indicates that there are two separated shells in the radial structure function (RSF). The first peak of the EXAFS spectra could be fitted to the first coordination shell of the Cu-O bond. While the second shell of the EXAFS spectra probably comes from Cu species interacting with TiO_2, indicating Cu_2O formation on TiO_2-NF surface confirmed STEM, and elemental mapping **(Fig. 3 a-g).**

Finally, surface area is an important factor for surface-related photoreaction, and the specific surface areas of the synthesized TiO_2-NF, Cu_2O, Cu_2O/TiO_2-NF samples were measured by nitrogen adsorption-desorption BET analysis as shown in **Fig. S7 a-g)**. The specific surface areas of pristine TiO_2-NF and Cu_2O were shown at 79.49 $m^2\ g^{-1}$ and 15.2 $m^2\ g^{-1}$, respectively. In particular, Cu_2O/TiO_2-NF composites were prepared under different temperatures from 50 to 100 °C. The surface areas were increased from 50 to 60 °C and then decreased gradually from 70 to 100 °C, which is due to the formation of particle size and aggregation of Cu_2O on the surface of TiO_2-NF. These results are well supported in the SEM and HRTEM images. The surface area and pore volume of synthesis products were calculated by the BET method, as summarised in **Table 1.** The high surface area and pore volume of the composites is beneficial for their photocatalytic activity.

3.2. Photocatalytic H_2 production

Fig. 7a-b shows the rates of photocatalytic H_2 generation of P25, Cu_2O, TiO_2-NF and Cu_2O/TiO_2-NF. Under UV-Vis light illumination for 8 h, the rates were 4.7 μmol $g^{-1}\ h^{-1}$ for P25, 7.2 μmol $g^{-1}\ h^{-1}$ for TiO_2-NF and 6.7 μmol $g^{-1}\ h^{-1}$ for Cu_2O. Meanwhile, the hydrogen production rates of Cu_2O/TiO_2-NF products were 34 μmol $g^{-1}\ h^{-1}$ for Cu_2O/TiO_2-NF (50°C), 48

μmol g^{-1} h^{-1} for both Cu_2O/TiO_2-NF (60 and 70°C), 36 μmol g^{-1} h^{-1} Cu_2O/TiO_2-NF (80 and 100°C). H_2 production rates of synthesised composites (~ 6.5 times higher compared with TiO_2-NF) were significantly enhanced. The reason could be the formation of the heterojunction at the interface between p-Cu_2O/n-TiO_2-NF, which will be discussed in details in later sections and also illustrated in **Scheme 2**. The apparent quantum efficiency (AQE) was calculated according to the previous methods[6, 18], and AQE of Cu_2O/TiO_2-NF (60°C) composites (~3.6%) significantly increased by a factor of ~6-fold compared with TiO_2-P25 and TiO_2-NF presented in Supporting information, **Fig. S8**. H_2 production and AQE of Cu_2O/TiO_2-NF synthesised at higher temperature (80 and 100°C) dropped slightly, probably due to the Cu_2O nanoparticles agglomerated on the TiO_2-NF surface.

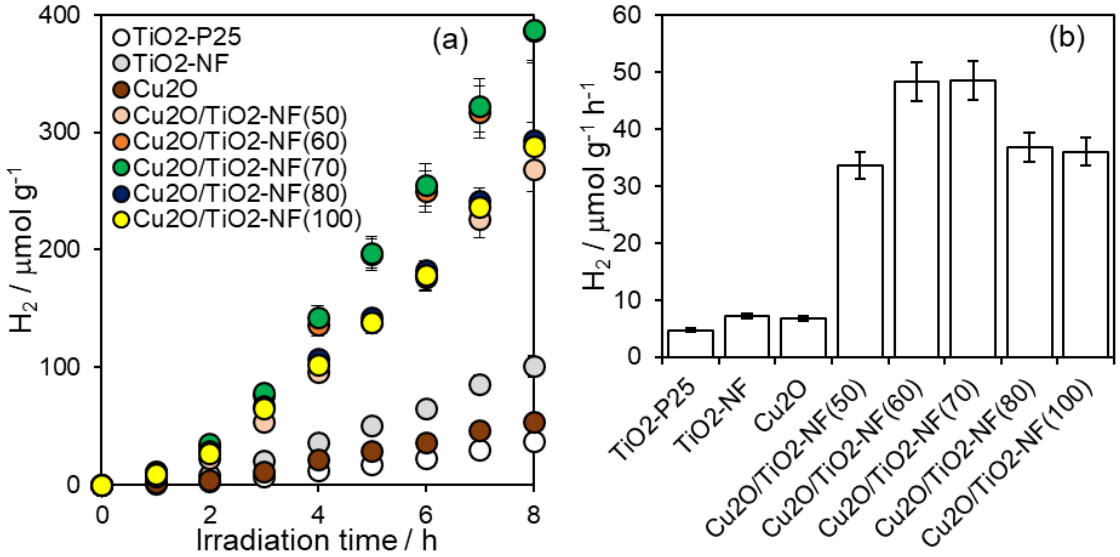

Fig. 7 a) Photocatalytic H_2 production amount and b) corresponding H_2 production rates over Cu_2O, TiO_2-P25, TiO_2-NF and their composites with methanol as a sacrificial electron donor.

In addition, we compared the H_2 generation rates of Cu_2O/TiO_2-NF (60 and 70°C) with other Cu_2O/TiO_2 composites and also noble metal modified TiO_2 composites. For various Cu_2O/TiO_2 composites, our Cu_2O/TiO_2-NF was more efficient (at least a factor of ~1.47) compared with previously reported core-shell nanowire arrays tested under UV irradiation with no AQE reported [33]. For a range of noble metal modified TiO_2 composites, comparison was summarised in **Table S2**. It is impossible to compare H_2 generation rates directly when the reaction set-ups are significantly different. However, it is very promising that Cu_2O/TiO_2-NF (using only cheap and earth abundant materials) shows comparable activity to many of the noble metal modified TiO_2 composites.

3.3. Photocatalytic sulfamethoxazole (SMX) oxidative degradation

The photocatalytic activity of Cu_2O/TiO_2-NF composites was also evaluated using SMX as an emerging antibiotic complex organic compound commonly used for both humans and animals worldwide for bacterial infections. The recent survey indicated that 59 t/year of SMX is used for animals and 24 t/year for humans in Japan [34]. Additionally, the discharges of SMX concentrations were unacceptable in the municipal and livestock wastewaters. In Europe, the discharged SMX concentration ranges from 0.01 to 2 μg L^{-1} in the municipal wastewater, and

the concentration varies in the surface waters from 0.03 to 0.48 μg L^{-1} [35]. The survey indicated that unacceptable SMX concentrations range from ng/L to μg/L in the United States [36]. The existence of antibiotic organics in the aqueous environment has a negative effect due to resistance to bacteria, resulting in the possibility of bacteria developing new resistant genes in the water bodies [37]. The present report was focused on the removal of persistent SMX pharmaceutical organic compounds (especially those low in concentration) under visible light.

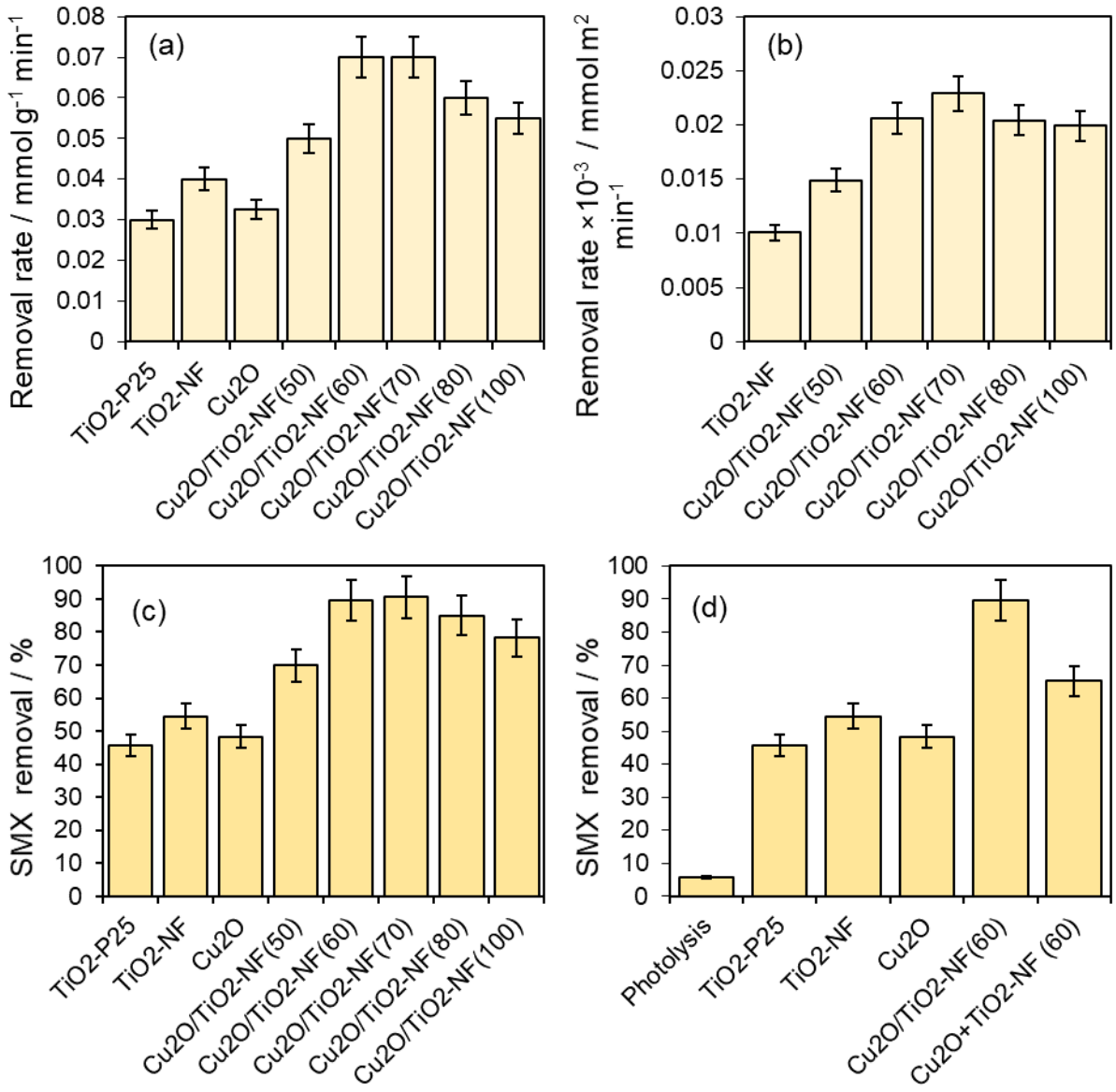

Fig. 8 a) photocatalytic initial removal rates of Sulfamethoxazole (SMX), b) corresponding area normalized rates (at 10 min), c) SMX photocatalytic degradation over synthesized Cu_2O, TiO_2 and Cu_2O/TiO_2-NF (60°C) catalyst, d) comparative SMX degradation efficiency over photolysis, TiO_2 Cu_2O, Cu_2O/TiO_2-NF (60°C) and Cu_2O+TiO_2-NF (60°C) physical mixture. Reaction conditions: 0.01184 mmol SMX; 50 mL of water; 20 mg of catalyst; reaction time of 10 min, corresponding degradation efficiency at 30 min.

The photocatalytic activity of as-synthesised Cu_2O, TiO_2-NF, Cu_2O/TiO_2-NF composites, as well as the physical mixture of Cu_2O+TiO_2-NF (60°C), was systematically applied for SMX

photodegradation under visible light as presented in **Fig. 9a-d**. The SMX organic molecule was intentionally selected in this study because it is not a dye molecule and it does not have visible light absorption ability. While if dye molecule was applied, it would be difficult to distinguish the catalytic mechanism initiated by either dyes or photocatalysts [38]. Initially, the 0.01184 mmol of SMX antibiotic organic molecule with synthesised photocatalysts (20 mg) were conducted for adsorption study for 1 h in a dark condition. Meanwhile, oxidation of SMX with light-only without any photocatalysts was checked, the removal rate was only 5.8 % of SMX, probably due to photolysis.

When TiO_2-P25, TiO_2-NF and Cu_2O were applied as photocatalysts, initial removal rates of SMX were 0.03, 0.04 and 0.03 mmol g^{-1} min^{-1} after 10 min, and the corresponding removal efficiencies were 45.7 %, 54.5 %, and 48.4 % after 30 min of reaction, respectively. SMX initial oxidation rates after 10 min and removal percentages after 30 min were much higher. Cu_2O/TiO_2-NF (60 and 70° C) showed the highest rates of 0.07 mmol g^{-1} min^{-1} and highest removal percentage 91%. In addition, the AQE was 35, 46, and 38% for TiO_2-P25, TiO_2-NF and Cu_2O, while Cu_2O/TiO_2-NF (60 and 70° C) showed the highest of 81%, as presented in **Fig. S9**. The photocatalytic activity was reduced beyond the optimal synthesis temperature (60 and 70° C) of Cu_2O, agreed with H_2 generation results.

Physical mixture of Cu_2O+TiO_2-NF was also tested for SMX degradation and showed 65% removal percentage after 30 min which is much lower than 91% of Cu_2O/TiO_2-NF (60° C). This indicates that the excellent photocatalytic activity in the composites might be an effective synergistic heterojunction followed by carrier charge transfer at Cu_2O to TiO_2-NF interfaces.

SMX removal over other reported TiO_2 based photocatalysts are summarised in **Table S3**. Again, it is not possible to compare reaction rates directly when the reaction set-ups are significantly different. However, it is very promising that Cu_2O/TiO_2-NF shows comparable activity under visible light only to many other photocatalysts with some of them were tested under UV light.

The photocatalytic removal of SMX and their oxidation by-products were investigated using HPLC (**Fig. S10-12)** and LC-MS/MS analysis (**Fig. S13** a-e). By-products and proposed pathway are presented in **Scheme 2**. The pathway might follow these subsequent steps: (I) $^{\bullet}OH$ radicals attack on the benzene ring with formation of hydroxylated SMX and aminophenol; which leads to the cleavage of the S-N bond; (II) deamination to form a nitro-substituted benzene ring, which further cleavage into C–N bonds in SMX; (III) The hydroxylated and deaminated SMX further cleavage of several C-S, C-N, S-N bonds in SMX (especially, isoxazole and benzene rings) [39-42]. The photocatalytic oxidation of SMX over Cu_2O/TiO_2-NF (60°C) eliminating C–S bond, cleavage of carbon-nitrogen (C-N) bond, various carbon-carbon (C–C) cleaved followed by $^{\bullet}OH$ radical attack for the aromatic ring opening in the sulfamethoxazole[43].

The total organic carbon (TOC) analysis of aqueous samples after SMX removal using Cu_2O/TiO_2-NF (60º C) was carried out. The photocatalytically degraded solutions at different time intervals were collected and analysed. In the dark conditions, the TOC elimination was only 3.4% and this was increased to 73.5% upon light irradiation of 30 min, indicating majority

of SMX was mineralised and the final reaction mixture might contain small amount of shorter carbonaceous molecules, e.g. the carboxylic acids as suggested in **Scheme 2**.

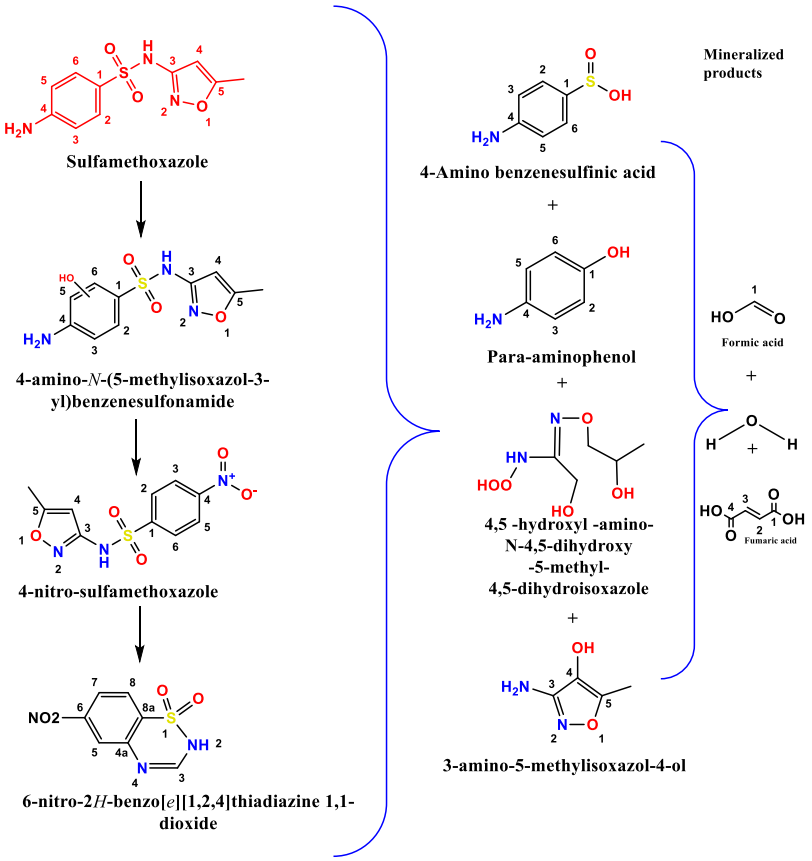

Scheme 2 Proposed by-product formation over Cu_2O/TiO_2-NF (60°C) catalysts.

The influence of •OH radical in this photocatalytic reaction was further verified by radical quenching experiments. The SMX removal rates were considerably low after the addition of isopropyl alcohol (IPA) and ethylenediaminetetraacetic acid (EDTA) which quenched •OH radical-mediated reaction as presented in **Fig. S14a**. The •OH radical-mediated SMX elimination over Cu_2O/TiO_2-NF (60°C) photocatalyst was also verified through the generation of •OH radicals, whose generation was confirmed using fluorescence spectroscopy with terephthalic acid (TA) used as the probe molecule. The 2-hydroxy terephthalic acid (2-HTA) formation via •OH radical attack is well established. Higher intensity of 2-HTA in the fluorescence spectrum confirmed the generation of •OH radical in this specific reaction (**Fig. S14b**).

3.4. Photoelectrochemical performance

The effect of interfacial Cu_2O/TiO_2-NF heterojunction on transfer of photogenerated charge carriers was investigated using transient photocurrent measurements under chopped light illumination. **Fig. 9a** shows that Cu_2O/TiO_2-NF (60°C) > TiO_2-NF > Cu_2O in terms of photocurrent response. The significantly increased photocurrent of Cu_2O/TiO_2-NF (60°C) heterojunction showed improved separation of electrons from holes and efficient charge transport across the interface compared to individual components.[44]. There are noticeable current overshoot when the light is switched off due to the continuing flux of electrons into the

surface as holes remaining in the surface states recombine. It is a widely observed phenomenon in photocurrent measurements, known as cathodic current overshoot or anomalous transient photocurrent [45, 46]. We believe the significant overshoot for Cu_2O/TiO_2-NF links to its unique structure and superior photocatalytic performance. We are still exploring some clearer insights because the overshoot current links to quite a few factors, e.g. surface defects/trap states, surface recombination, hole transfer, band alignment and bending, etc.

Electrochemical impedance spectroscopy illustrates the characteristics of the charge transfer process, and the semicircle diameter indicates the charge transfer resistance [47]. From **Fig. 9b**, the charge transfer resistance of Cu_2O/TiO_2-NF (60°C) catalysts was smaller than those of TiO_2-NF and Cu_2O, which implies that the p-n heterojunction formation between Cu_2O and TiO_2-NF improves electron migration and increases the conductivity for enhanced electron transfer to active sites on the catalyst surface.

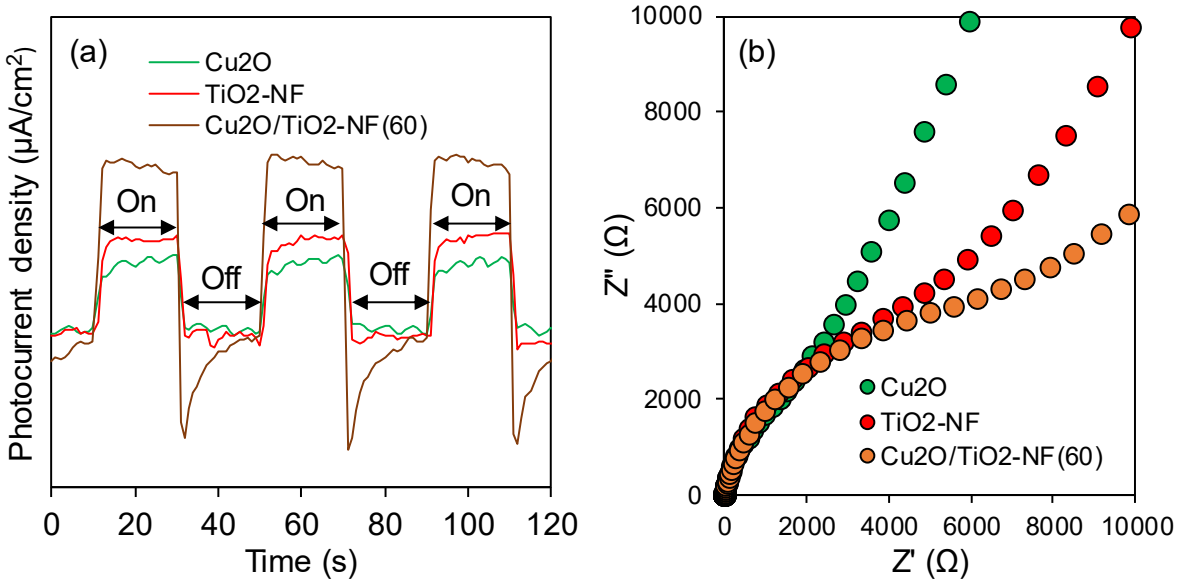

Fig. 9 a) Transient photocurrent, b) Electrochemical Impedance Spectroscopy (EIS).

3.5. Band energy alignment at the interface of Cu_2O/TiO_2-NF heterojunction

The band alignment between the p-Cu_2O/n-TiO_2-NF heterojunction interface can be calculated based on a well-established method described in the below **eqs (5)** and **(6)** [15, 48, 49]:

$$\Delta E_V = \left(E_{Ti2P}^{Cu2O/TiO2-NF} - E_{Cu2p}^{Cu2O/TiO2-NF}\right) + \left(E_{Cu2p}^{Cu2O} - E_{VBM}^{Cu2O}\right) - \left(E_{Ti2p}^{TiO2-NF} - E_{VBM}^{TiO2-NF}\right) \quad \mathbf{5}$$

$$\Delta E_c = \Delta E_V + E_g^{Cu2O} - E_g^{TiO2-NF} \quad \mathbf{6}$$

Where $\left(E_{Ti2P}^{Cu2O/TiO2-NF} - E_{Cu2p}^{Cu2O/TiO2-NF}\right)$ indicates the core-level (CL) difference in energy between Ti2p and Cu2p obtained from the Cu_2O/TiO_2-NF heterojunction; meanwhile, $(E_{Cu2p}^{Cu2O} - E_{VBM}^{Cu2O})$ and $\left(E_{Ti2p}^{TiO2-NF} - E_{VBM}^{TiO2-NF}\right)$ indicates the core-level as well as valency-band maximum energies in the Ti2p and Cu2p counterpart. $E_g^{Cu2O} - E_g^{TiO2-NF}$ indicates the

band gap difference of Cu_2O and TiO_2 materials. ΔE_V and ΔE_c are the valence band and conduction band offset in the Cu_2O/TiO_2-NF (60°C) heterojunction.

All the values needed for **eqs (5)** and **(6)** come from XPS and UV-Vis measurements, the calculated ΔE_V is 1.76 eV and ΔE_c is 0.72 eV, which are consistent with similar previous reports [15, 48, 49], and presented in **Scheme 3**. From the band alignment, we can learn that the formation of p-Cu_2O/n-TiO_2-NF heterojunction leads to build in electric field and space-charge regions followed by band bending, which is a great advantage to enhance electron transfer across the p-Cu_2O/n-TiO_2-NF interface for higher catalytic activity [50].

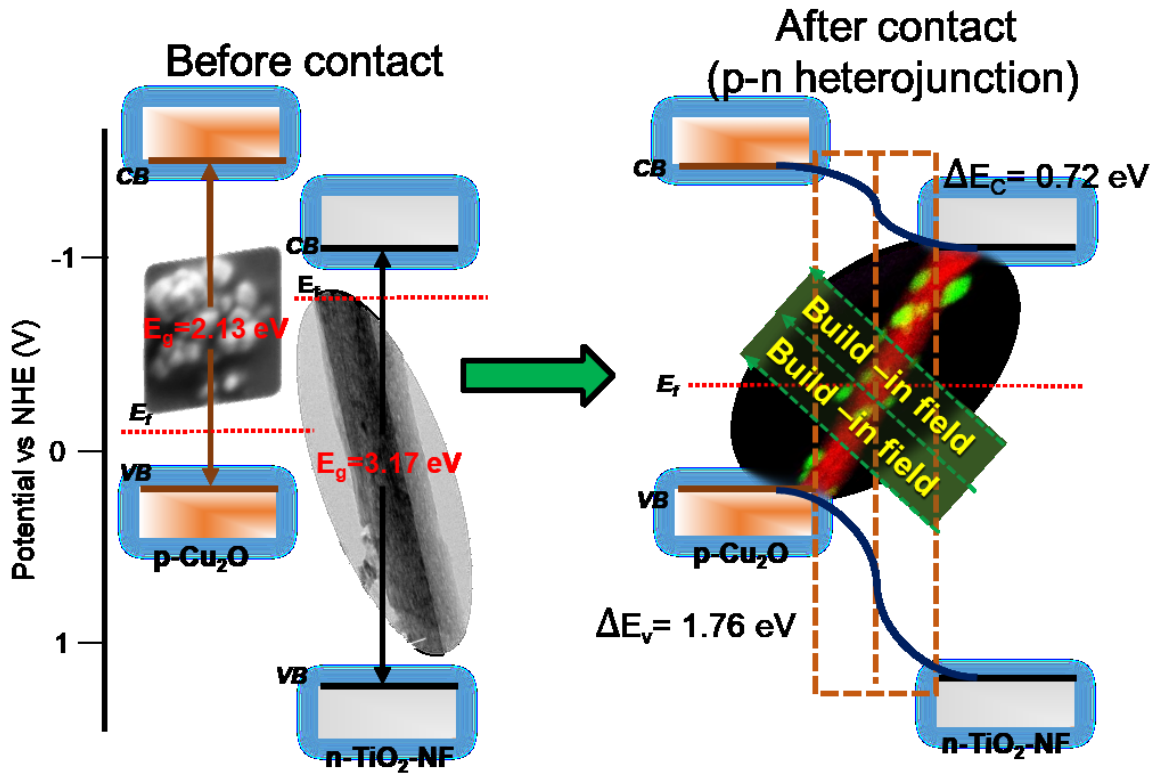

Scheme 3. Band alignment energy diagram of Cu_2O, TiO_2-NF before and after contact. (CB: conduction band, VB: valence band, E_f: Fermi level, ΔE_C: conduction bands offset, ΔE_V: valence bands offset.)

3.6. Catalyst durability

Catalyst durability is an important parameter for photocatalytic application, and in the present report, we have conducted the SMX degradation over Cu_2O/TiO_2-NF (60°C) catalysts for five cycles. The multi-cycle test indicated that the SMX degradation percentage was not changed even after five cycles, and the synthesised Cu_2O/TiO_2-NF (60°C) nanocomposite exhibiting high activity and excellent stability for photocatalytic applications.

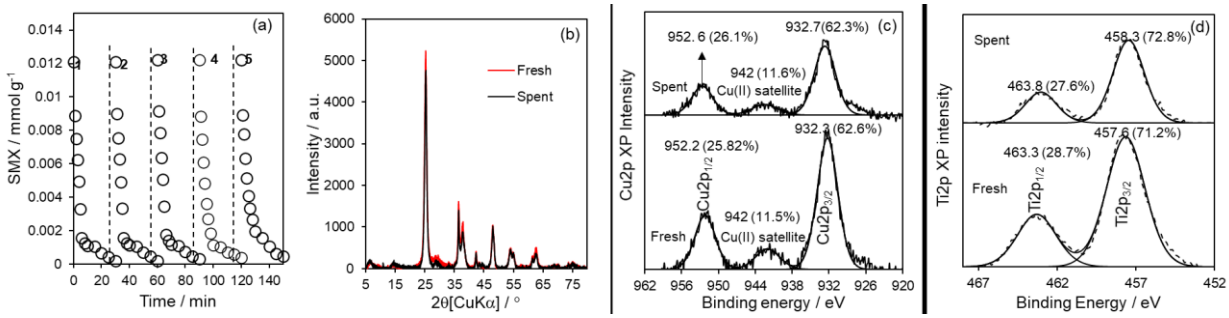

Fig. 10 a) Catalyst stability by recycle experiments, b) XRD patterns, c) and d) XPS spectrum, of fresh and spent Cu_2O/TiO_2-NF (60°C).

In addition, Cu_2O is normally unstable under light irradiation, and surprisingly, the TiO_2-NF structure enhances the photo stability and slows down the oxidation and aggregation of Cu_2O nanoparticles, evidenced by spent catalyst XRD, XPS and electron microscopy studies as presented in **Fig. 10** and **Fig. S15a-f**. Negligible changes in crystal phase, oxidation states and morphologies were observed over five consecutive cycles of SMX degradation under visible light illumination.

Last but not least, recovery and collection of fine catalyst particles in colloidal suspension is highly challenging for the photocatalytic application. However, because of the large overall size of Cu_2O/TiO_2-NF composite, the Cu_2O/TiO_2-NF can be easily separated from the post-reaction mixture of the SMX using simple precipitation after 1 h.

4. Conclusion

We demonstrated a simple synthetic approach for the construction of p-Cu_2O/n-TiO_2-NF synergistic photocatalyst for both H_2 production and organic decomposition applications with high durability. The simple strategy (low hydrothermal 60°C) constructed ultrafine Cu_2O (20-100 nm) nanoparticles partially submerged on the TiO_2 nanofibre (diameter ~300 nm and length ~650 nm) architecture, which significantly improved the surface electronic and optical properties, as well as displayed excellent synergistic visible light photocatalysis. Deeper insights of interfacial heterojunction formation and charge carrier transfer are their relationship with enhanced photocatalytic performance were evidenced and discussed in detail. Overall, the results not only offer a better photocatalyst for environmental remediation but also provide physical insights for further development of noble-metal-free concept for photocatalytic H_2 evolution and other solar energy conversion applications.

Supporting information

Material characterization, **Fig. S1** FE-SEM images of synthesised Cu_2O, TiO_2-NF and Cu_2O/TiO_2-NF (60°C). **Fig. S2** a-e) FE-SEM images of Cu_2O/TiO_2-NF at different temperature (50 to 100°C), **Fig. S3** a-e) HR-TEM images of synthesised Cu_2O/TiO_2-NF (60°C) captured an Orius camera, **Fig. S4** Solid state DR UV-vis spectra (Tauc plot) of Cu_2O, TiO_2 and their

composites (50 to 100°C), **Fig. S5** a-f) XPS spectra of Cu 2p, and Ti 2p of Cu_2O, TiO_2 and Cu_2O/TiO_2-NF composites (50 to 100°C), **Fig. S6** Cu K-edge EXAFS spectra of Cu_2O/TiO_2-NF (50 to 100°C) in k space, **Table S1** XANES linear combination fitting of Cu_2O, Cu_2O/TiO_2-NF composites, **Fig. S7** a-g) N_2 adsorption-desorption isotherm of Cu_2O, TiO_2 and their composites (50 to 100°C), **Fig. S8** Apparent quantum efficiency of H_2 production over Cu_2O, TiO_2-P25, TiO_2-NF and their composites, **Fig. S9** Apparent quantum efficiency of SMX removal over Cu_2O, TiO_2-P25, TiO_2-NF and their composites, **Fig. S10** a-b) HPLC reaction mixture of before and after photocatalytic SMX degradation over Cu_2O/TiO_2-NF (50 and 60°C), **Fig. S11** a-b) HPLC reaction mixture of before and after photocatalytic SMX degradation over Cu_2O/TiO_2-NF (70 and 80°C), **Fig. S12** HPLC reaction mixture of before and after photocatalytic SMX degradation over Cu_2O/TiO_2-NF (100°C), **Fig. S13**. a) LC-MS/MS spectra of SMX, **Fig. S13**. b) LC-MS/MS spectra of SMX products (5 min) over Cu_2O/TiO_2-NF (60°C) catalyst, **Fig. S13**. c) LC-MS/MS spectra of SMX products (10 min) over Cu_2O/TiO_2-NF (60°C) catalyst, **Fig. S13**. d) LC-MS/MS spectra of SMX products (20 min) over Cu_2O/TiO_2-NF (60°C) catalyst, **Fig. S13**. e) LC-MS/MS spectra of SMX products (30 min) over Cu_2O/TiO_2-NF (60°C) catalyst, **Fig. S14** a) Influence of SMX removal rates by trapping agent addition over Cu_2O/TiO_2-NF (60°C), b) PL emission spectra of HTA as a function of time over Cu_2O/TiO_2-NF (60 °C), **Fig S15** a-b) Fresh and spent SEM of Cu_2O/TiO_2-NF (60 ºC), c-d) fresh HRTEM and e-f) Spent HR-TEM of Cu_2O/TiO_2-NF (60 ºC), **Fig. S16** Wavelength distribution of the Xenon lamp light source.

Conflicts of interest

The authors declare no conflict of interest.

ACKNOWLEDGMENTS

S. K. and K. S. would like to thank the Japan Society for the Promotion of Science (JSPS) for providing a postdoctoral fellowship for foreign researchers (P18387) and the research grant (KAKENHI JP18F18387). We acknowledge for the EC H2020 Marie S Curie RISE award (871998) and the Chinese Inter-governmental National Sci & Tech Innovation Cooperation (2019YFE0197500). XANES measurements were performed at Kyushu University Beamline (SAGA-LS/BL06 with proposal No. 2019IIIK005). FE-SEM and HR(S)TEM performed at the Ultra-microscopy Research Centre (URC) at Kyushu University. This work was partly supported by Nanotechnology Platform Program (Molecule and Material Synthesis) of the Ministry of Education, Culture, Sports, Science and Technology (MEXT), Japan.

References

[1] B.-H. Lee, S. Park, M. Kim, A.K. Sinha, S.C. Lee, E. Jung, W.J. Chang, K.-S. Lee, J.H. Kim, S.-P. Cho, Nature materials 18 (2019) 620-626.

[2] A. Fujishima, T.N. Rao, D.A. Tryk, Journal of Photochemistry and Photobiology C: Photochemistry Reviews 1 (2000) 1-21.

[3] W.-K. Jo, S. Kumar, M.A. Isaacs, A.F. Lee, S. Karthikeyan, Applied Catalysis B: Environmental 201 (2017) 159-168.

[4] Y. Liu, B. Zhang, L. Luo, X. Chen, Z. Wang, E. Wu, D. Su, W. Huang, Angewandte Chemie International Edition 54 (2015) 15260-15265.
[5] M. Schreier, J. Luo, P. Gao, T. Moehl, M.T. Mayer, M. Grätzel, Journal of the American Chemical Society 138 (2016) 1938-1946.
[6] K. Sekar, C. Chuaicham, U. Balijapalli, W. Li, K. Wilson, A.F. Lee, K. Sasaki, Applied Catalysis B: Environmental 284 119741.
[7] Z. He, J. Fu, B. Cheng, J. Yu, S. Cao, Applied Catalysis B: Environmental 205 (2017) 104-111.
[8] Y.A. Wu, I. McNulty, C. Liu, K.C. Lau, Q. Liu, A.P. Paulikas, C.-J. Sun, Z. Cai, J.R. Guest, Y. Ren, V. Stamenkovic, L.A. Curtiss, Y. Liu, T. Rajh, Nature Energy 4 (2019) 957-968.
[9] L. Wan, Q. Zhou, X. Wang, T.E. Wood, L. Wang, P.N. Duchesne, J. Guo, X. Yan, M. Xia, Y.F. Li, A.A. Jelle, U. Ulmer, J. Jia, T. Li, W. Sun, G.A. Ozin, Nature Catalysis 2 (2019) 889-898.
[10] M. Wang, L. Sun, Z. Lin, J. Cai, K. Xie, C. Lin, Energy & Environmental Science 6 (2013) 1211-1220.
[11] A. Dhakshinamoorthy, S. Navalon, A. Corma, H. Garcia, Energy & Environmental Science 5 (2012) 9217-9233.
[12] M. Wang, L. Sun, Z. Lin, J. Cai, K. Xie, C. Lin, Energy & Environmental Science 6 (2013) 1211-1220.
[13] T. Wei, Y.-N. Zhu, X. An, L.-M. Liu, X. Cao, H. Liu, J. Qu, ACS Catalysis 9 (2019) 8346-8354.
[14] X. Xu, Z. Gao, Z. Cui, Y. Liang, Z. Li, S. Zhu, X. Yang, J. Ma, ACS applied materials & interfaces 8 (2016) 91-101.
[15] L. Liu, W. Yang, W. Sun, Q. Li, J.K. Shang, ACS applied materials & interfaces 7 (2015) 1465-1476.
[16] Y. Bai, W. Li, C. Liu, Z. Yang, X. Feng, X. Lu, K.-Y. Chan, Journal of Materials Chemistry 19 (2009) 7055-7061.
[17] S. Karthikeyan, S. Kumar, L.J. Durndell, M.A. Isaacs, C.M. Parlett, B. Coulson, R.E. Douthwaite, Z. Jiang, K. Wilson, A.F. Lee, ChemCatChem 10 (2018) 3554-3563.
[18] S. Karthikeyan, C. Chuaicham, R.R. Pawar, K. Sasaki, W. Li, A.F. Lee, K. Wilson, Journal of Materials Chemistry A 7 (2019) 20767-20777.
[19] S. Karthikeyan, K. Ahmed, A. Osatiashtiani, A.F. Lee, K. Wilson, K. Sasaki, B. Coulson, W. Swansborough-Aston, R.E. Douthwaite, W. Li, ChemCatChem 12 (2020) 1699-1709.
[20] C.-H. Kuo, C.-H. Chen, M.H. Huang, Advanced Functional Materials 17 (2007) 3773-3780.
[21] L. Gou, C.J. Murphy, Nano Letters 3 (2003) 231-234.
[22] S. Sun, Z. Yang, Chemical Communications 50 (2014) 7403-7415.
[23] H. Yu, J. Yu, S. Liu, S. Mann, Chemistry of Materials 19 (2007) 4327-4334.
[24] C. Chuaicham, S. Karthikeyan, R.R. Pawar, Y. Xiong, I. Dabo, B. Ohtani, Y. Kim, J.T. Song, T. Ishihara, K. Sasaki, Chemical Communications 56 (2020) 3793-3796.
[25] C. Chuaicham, S. Karthikeyan, J.T. Song, T. Ishihara, B. Ohtani, K. Sasaki, ACS Applied Materials & Interfaces 12 (2020) 9169-9180.
[26] J. Lv, C. Kong, K. Liu, L. Yin, B. Ma, X. Zhang, S. Yang, Z. Yang, Chemical Communications 54 (2018) 8458-8461.
[27] M. Schulz-Dobrick, K.V. Sarathy, M. Jansen, Journal of the American Chemical Society 127 (2005) 12816-12817.
[28] X. Qiu, M. Miyauchi, K. Sunada, M. Minoshima, M. Liu, Y. Lu, D. Li, Y. Shimodaira, Y. Hosogi, Y. Kuroda, Acs Nano 6 (2012) 1609-1618.
[29] C.H. Kuo, C.H. Chen, M.H. Huang, Advanced Functional Materials 17 (2007) 3773-3780.
[30] W. Zou, L. Zhang, L. Liu, X. Wang, J. Sun, S. Wu, Y. Deng, C. Tang, F. Gao, L. Dong, Applied Catalysis B: Environmental 181 (2016) 495-503.
[31] H. Azimi, S. Kuhri, A. Osvet, G. Matt, L.S. Khanzada, M. Lemmer, N.A. Luechinger, M.I. Larsson, E. Zeira, D.M. Guldi, C.J. Brabec, Journal of the American Chemical Society 136 (2014) 7233-7236.

[32] M. Yin, C.-K. Wu, Y. Lou, C. Burda, J.T. Koberstein, Y. Zhu, S. O'Brien, Journal of the American Chemical Society 127 (2005) 9506-9511.
[33] L. Yao, W. Wang, L. Wang, Y. Liang, J. Fu, H. Shi, International Journal of Hydrogen Energy 43 (2018) 15907-15917.
[34] A. Murata, H. Takada, K. Mutoh, H. Hosoda, A. Harada, N. Nakada, Science of the total Environment 409 (2011) 5305-5312.
[35] A.G. Trovó, R.F.P. Nogueira, A. Agüera, A.R. Fernandez-Alba, C. Sirtori, S. Malato, Water Research 43 (2009) 3922-3931.
[36] D.W. Kolpin, E.T. Furlong, M.T. Meyer, E.M. Thurman, S.D. Zaugg, L.B. Barber, H.T. Buxton, Environmental Science & Technology 36 (2002) 1202-1211.
[37] S. Wang, J. Wang, Chemosphere 191 (2018) 97-105.
[38] N. Barbero, D. Vione, Environmental Science & Technology 50 (2016) 2130-2131.
[39] A. Wang, Y.-Y. Li, A.L. Estrada, Applied Catalysis B: Environmental 102 (2011) 378-386.
[40] S. Wang, J. Wang, Chemical Engineering Journal 351 (2018) 688-696.
[41] A. Kumar, A. Kumar, G. Sharma, H. Ala'a, M. Naushad, A.A. Ghfar, F.J. Stadler, Chemical Engineering Journal 334 (2018) 462-478.
[42] H.Y. Kim, T.-H. Kim, S.M. Cha, S. Yu, Chemical Engineering Journal 313 (2017) 556-566.
[43] A.G. Trovó, R.F. Nogueira, A. Agüera, A.R. Fernandez-Alba, C. Sirtori, S. Malato, Water research 43 (2009) 3922-3931.
[44] S.J. Moniz, S.A. Shevlin, D.J. Martin, Z.-X. Guo, J. Tang, Energy & Environmental Science 8 (2015) 731-759.
[45] C.Y. Cummings, F. Marken, L.M. Peter, A.A. Tahir, K.G.U. Wijayantha, Chemical Communications 48 (2012) 2027-2029.
[46] L. Hu, X. Liu, S. Dalgleish, M.M. Matsushita, H. Yoshikawa, K. Awaga, Journal of Materials Chemistry C 3 (2015) 5122-5135.
[47] Y. Wu, T. Livneh, Y.X. Zhang, G. Cheng, J. Wang, J. Tang, M. Moskovits, G.D. Stucky, Nano Letters 4 (2004) 2337-2342.
[48] M.E. Aguirre, R. Zhou, A.J. Eugene, M.I. Guzman, M.A. Grela, Applied Catalysis B: Environmental 217 (2017) 485-493.
[49] C. Jia, Y. Chen, X. Zhou, A. Yang, G. Zheng, X. Liu, S. Yang, Z. Wang, Applied Physics A 99 (2010) 511-514.
[50] B. Long, H. Yang, M. Li, M.-S. Balogun, W. Mai, G. Ouyang, Y. Tong, P. Tsiakaras, S. Song, Applied Catalysis B: Environmental 243 (2019) 365-372.